Materials Research Bulletin 179 (2024) 112955

Contents lists available at ScienceDirect

Materials Research Bulletin

journal homepage: www.elsevier.com/locate/matresbu

Research Papers

Enhancing photoelectrocatalytic efficiency by tuning graphitic carbon nitride characteristics for production of heterojunctions with W-$BiVO_4$

Caroline H. Claudino [a], Marcos R.S. Vicente [a], Maria Kuznetsova [b], José M. De Carvalho [a], Juliana S Souza [*,a]

[a] Centro de Ciências Naturais e Humanas, Universidade Federal do ABC, Avenida dos Estados, 5001, zip code 09210-580, Santo André, Brazil
[b] Centro de Lasers e Aplicações, CNEN-IPEN/SP, Av. Prof. Lineu Prestes 2242, zip code 05508-000, São Paulo, Brazil

ARTICLE INFO

Keywords:
Graphitic carbon nitride
Bismuth vanadate
Microwave synthesis
Metal oxide semiconductor
Water splitting

ABSTRACT

The escalating interest in utilizing solar energy for photocatalytic applications to address energy crises has spurred extensive research in developing efficient systems. Monoclinic $BiVO_4$ is known for its superior photocatalytic capabilities; however, challenges like a high recombination rate and an unsuitable conduction band potential for the hydrogen evolution reaction limit its application. To overcome these challenges, doping $BiVO_4$ with W (WB) and forming heterojunctions with graphitic carbon nitride (g-C_3N_4) are promising strategies to reduce charge recombination and increase visible light sensibility. This study shows that the hydrothermal treatment of g-C_3N_4 modifies its morphology and interaction with $BiVO_4$ and W-$BiVO_4$. Notably, our findings reveal a significant difference in the photoresponse between the combination of W-$BiVO_4$ with g-C_3N_4, produced upon hydrothermal treatment (MHWB), and the combination with g-C_3N_4 produced without hydrothermal treatment (MDWB). The MHWB combination enhances the photoresponse by twice. Also, MHWB shows a higher activity for photocatalytic degradation of tetracycline.

1. Introduction

The interest in using solar energy for photocatalytic processes has grown, as it is an up-and-coming solution for energy crises [1,2]. A system that has attracted much attention is the $BiVO_4/C_3N_4$ heterojunction due to its photocatalytic advantages and applications, which include water pollutant degradation, water splitting, and carbon dioxide reduction [3,4].

$BiVO_4$ is attractive due to its low band-gap energy (2.40 eV), sensitivity to visible light, good chemical stability, and low toxicity [3–6]. However, its high recombination rate of photogenerated charges and the fact that its conduction band potential is unsuitable for hydrogen evolution reaction limits its application [3–7].

To overcome the abovementioned issue, an interesting strategy is doping $BiVO_4$ with Mo^{6+} or W^{6+}. This strategy is interesting because it can adjust the electrical properties and Fermi's level of semiconductors, as these ions are electron donors and can interact efficiently with $BiVO_4$ [8].

Formation of heterojunction with materials sensitive to visible light, such as $Fe_2O_3/BiVO_4$ [9], $NiO/BiVO_4$ [10], $MnO_2/BiVO_4$ [11], etc. Graphitic carbon nitride (g-C_3N_4) has emerged as a promising material for producing this heterojunction. The g-C_3N_4 is an organic semiconductor of low band-gap energy and, therefore, sensitivity to visible light [3,5–7,12]. Unlike other organic semiconductors, its lamellar structure makes it chemically and thermally stable [3,5–7,12]. The potential of the conduction band of C_3N_4 is very negative, which yields photo-excited electrons that can form superoxide radicals, which improve oxygen reactions for the degradation of pollutants [3]. In addition, the heterojunction with $BiVO_4$ causes the bands to align, which enhances this charge transfer [5].

The most common routes to synthesizing graphitic carbon nitride involve thermal methods through pyrolysis of urea, melamine, and dicyandiamide [13,14]. Typically, the procedures require calcination temperature varying from 500 to 550 °C [13,15–19] in one or two steps [15,18], from 2 to 4 h [13,14,16,17]. Hydrothermal methodologies have been little investigated [20–22]. The resultant particles exhibit irregular shapes [15,16], nanosheets [17–19], layered wrinkled structures of g-C_3N_4 [23], fractal layered structures [24], and tubular [25].

Combining the produced g-C_3N_4 with $BiVO_4$ typically involves two steps: first, synthesizing graphitic carbon nitride via thermal

* Corresponding author at: Federal University of the ABC, Brazil.
E-mail address: juliana.souza@ufabc.edu.br (J.S. Souza).

https://doi.org/10.1016/j.materresbull.2024.112955
Received 18 January 2024; Received in revised form 9 May 2024; Accepted 16 June 2024
Available online 19 June 2024

polymerization. Subsequently, the heterojunction is formed by introducing the prepared g-C_3N_4 into the reaction media to synthesize $BiVO_4$ through hydrothermal methods [3,6,7,12], ultrasound-assisted method [5], microwave method [4], ultrasonic dispersion method [23] and other cost-effective methods [19]. These methods allow the synthesis of different morphologies for the same material, thus increasing its efficiency for each type of application.

Here, we show how hydrothermal treatment can enhance the efficiency of the W-$BiVO_4$/ g-C_3N_4 system by modifying the characteristics of graphitic carbon nitride. Also, we show that doping $BiVO_4$ with tungsten results in a more efficient heterojunction. Hydrothermal treatment of melamine before the calcination procedure can affect the characteristics of the resultant g-C_3N_4 and, consequently, the photo (electro)catalytic efficiency of $BiVO_4$/C_3N_4 and W-$BiVO_4$/C_3N_4 heterojunctions. It has been observed that the obtaining method of g-C_3N_4 plays an essential role in the charge transfer efficiency of the different heterojunctions.

2. Experimental

2.1. Hydrothermal synthesis of g-C_3N_4

The synthesis of g-C_3N_4 was carried out following the route described by Song and co-workers [20,21]. 3 g of melamine was added to 50 mL of MilliQ water. The mixture was kept under stirring for 30 min at room temperature. Then, the solution was transferred to a PTFE (Polytetrafluoroethylene) liner, filling 50 % of its volume. The system was positioned inside a stainless-steel autoclave and inserted into a muffle furnace. The reaction was kept for 24 h at 180 °C with a heating rate of 10 °C min^{-1}. After natural cooling, the material was centrifuged, washed twice with MilliQ water, and dried at 60 °C in an oven. Finally, the solid was calcined at 550 °C for 4 h in a closed system. The resultant material was named as MH (Hydrothermal Method).

2.2. Direct calcination of melamine

To verify whether the hydrothermal treatment of melamine influences the properties of g-C_3N_4, 1.5 g of melamine was calcined at 550 °C for 4 h in a closed system. The resulting material was named MD (Direct Calcination of Melamine).

2.3. Synthesis of tungsten-doped bismuth vanadate nanostructures (WB) and g-C_3N_4 composite

$BiVO_4$ (B) and tungsten-doped $BiVO_4$ (WB) synthesis followed the procedure previously described by our group [26].

First, 20 mL of $Bi(NO_3)_3$ and NH_4VO_3 0.1 mol L^{-1} solutions were prepared using ethanol as a solvent; the two solutions were stirred for 20 min. Then, the NH_4VO_3 solution was added dropwise to the $Bi(NO_3)_3$ solution. To prepare tungsten-doped bismuth vanadate (WB), ammonium metatungstate ($(NH_4)_6H_2W_{12}O_{40}$) was added to the solution with a weight percentage of W at 3 %. The use of a capping agent was investigated by adding 1 M in monomeric units of PVP (average mol wt 40,000). The resultant mixture was stirred for 30 min. Finally, the apparent pH was adjusted to 5 or 6 by adding NH_4OH aqueous solution, and the mixture was stirred for another 15 min.

The final mixture was transferred to a round-bottom glass, and MD and MH were added at a ratio of 60% wt; this ratio was chosen based on a previously reported method [4]. The flask was coupled to a reflux apparatus and placed in the cavity of a monomode microwave reactor (Discover-CEM). Materials were irradiated using 100 W of microwave power and kept at 78 °C for 30 min.

The resultant material was transferred to a tube and centrifuged thrice for 5 min and 4000 rpm. After each centrifugation, the supernatant was removed, and the solid was rinsed with ethanol. Finally, the samples were dried in the lab oven at 80 °C for 24 h. The final materials were labeled MHWB and MDWB.

Composites were also prepared using non-doped bismuth vanadate (B), which were obtained through the same procedure described above, without the addition of ($(NH_4)_6H_2W_{12}O_{40}$). The resultant materials were labeled as MHB and MDB.

2.4. Characterization

Scanning Electron Microscopy images (SEM) were collected on two scanning electron microscopes, FESEM JMS-6701F, JEOL and Neoscope JCM-5000, JEOL. The samples were analyzed using the pulverized solids fixed on the sample holder using conductive carbon tape. Transmission electron microscopy (TEM) characterization of the synthesized materials was performed on a Talos F200X G2 TEM operated at 200KV and a cold field emission gun (FEG-X). X-ray diffractograms were collected in the D8 Focus diffractometer (Bruker) with a Cu Kα radiation source operating at 40 kV and 40 mA. To perform the experiment, first, the samples were pulverized and suspended in ethanol; then, the suspension was dripped into a silicon slab and dried at room conditions for 24 h. The crystal structures of the materials were also evaluated by Raman spectroscopy, using a labRam HR Evolution (HORIBA) spectrometer using a 785 nm laser. The diffuse reflectance spectra were collected using a Cary 50Scan spectrometer (Varian) coupled to a fiber optic accessory (Pike). Zeta potential was measured on a Zetasizer NanoZS zeta potential analyzer (Malvern) at 25 °C. 1 mg of each catalyst was added to 5 mL of isopropanol and sonicated for 30 min. Then, 1 mL aliquot of the resultant suspension was transferred to a falconet, and the volume was completed to 10 mL with MilliQ water. The dependence of zeta potential on pH was evaluated using suspension with pH ranging from 3 to 10, which has been adjusted with aqueous solutions of HNO_3 and NH_4OH. Aliquots of 0.8 mL of each suspension were transferred to a DTS1070 cuvette and inserted into the equipment for analysis. Fourier-transform infrared spectroscopy (FTIR) spectra were collected using a 640-IR-FT Varia Fourier transform infrared spectrometer (Agilent) operating with micro-ATR (Ge crystal), using the prepared samples. TGA Q500 equipment was used for the TGA measurements, where samples weighing approximately 20 mg were placed in a platinum sample holder. A flow of 60 mL min^{-1} of N_2 was used, with an initial temperature of 0 °C, a final temperature of 400 °C, and a heating rate of 10 °C min^{-1}.

The photoluminescence measurements were performed in an FS5 Spectrofluorometer (Edinburgh Instruments) equipped with a 450 W Xenon lamp equipped with singular monochromators at the excitation and emission optics. All spectra shown were corrected for the intensity profile of the Xenon lamp and detection response.

2.5. Photoelectrochemistry

First, the samples were immobilized on conductive FTO substrates (fluorine-doped tin oxide ~7Ω cm^{-2}, Sigma). The FTO substrates were washed by soaking the slide in acetone, water, and ethanol; each solvent was sonicated for 15 min; the procedure was repeated three times. Suspensions of 1 mg mL^{-1} of each catalyst were prepared in 1-Propanol, and then 0.025 mL of Nafion was added. The suspensions were sonicated for 30 min. Finally, the material was deposited by dripping two 0.025 mL of prepared suspension onto the conducting substrate, allowing the solvent to evaporate after each drip. After drying the films, linear voltammetry measurements were performed in the presence and absence of simulated sunlight. The electrochemical measurements were performed using a three-electrode system in a cell with a quartz window. FTO films were used as working electrodes, Ag/AgCl as the reference electrode and a Pt wire as the counter electrode. An aqueous solution of 0.2 M Na_2SO_4 and an aqueous solution of 0.1 M Na_2SO_4 10 % buffer pH 7 were used as the electrolytes. The system was positioned at a fixed distance from a solar simulator with a filter suitable for simulating sunlight with an A.M. 1.5 G spectrum at an intensity of 100 mW cm^{-2}, power measured with a Newport model 842-PE power meter coupled to an 818-P-001–12 light

intensity detector.

IPCE spectra were obtained using a Newport system. This system consists of a 300 W Xe lamp (model 6258) placed in a lamp housing that illuminates the entrance slit of a 0.25 m Czerny–Turner monochromator (Cornerstone 260), which has a diffraction grating of 1200 lines mm^{-1} and band-pass filters to avoid second-order effects. The *quasi*-monochromatic light beam exits the monochromator, and a beam-splitter splits the incident light to the sample and a silicon detector, model 818-UV, which was connected to a virtual power meter, model 841-p-USB. For comparison, an electrode made of commercial P25 (Sigma Aldrich - nanopowder, <25 nm particle size) was prepared similarly and evaluated as a photocatalyst.

2.6. Photocatalysis

The photocatalytic activity of the samples was investigated according to the procedure described in the literature [27]. First, it was prepared a solution of 10 mg L^{-1} tetracycline (TC), then 3 mg of photocatalyst (B, WB, MH, MHB, MHWB, MD, MDB, MDWB) was added into 10 ml of TC aqueous solution and stirred in the dark for 30 min to ensure the adsorption equilibrium. The system was positioned at a fixed distance from a solar simulator with a filter suitable for simulating sunlight with an A.M. 1.5 G spectrum at an intensity of 100 mW cm^{-2}, power measured with a Newport model 842-PE power meter coupled to an 818-P-001–12 light intensity detector. An aliquot of the suspension was taken out at intervals of 15 min for 1 hour. The concentration of TC was analyzed by a UV–vis spectroscopy monitoring λ_{max} = 357 nm. For comparison, commercial P25 was also evaluated as a photocatalyst.

3. Results and discussion

3.1. Characterization

Scanning electron microscopy images (Fig. 1) were acquired to investigate the morphology of the prepared materials. Pure $BiVO_4$ (B) and $WBiVO_4$ (WB) were prepared and characterized previously by the group [26]. SEM images of B and WB are reproduced in Fig. 1 (with permission), where it is possible to observe that B is composed of irregular particles surrounded by a layer of polymeric appearance, which is ascribed to a PVP layer. For the WB, the formation of small square structures that self-organize into larger squares is observed.

The SEM image of MH shows that this species has a sharp surface appearance with no evidence of nanostructured or controlled morphology. Song and collaborators [20] observed the same aspect, obtaining C_3N_4 through hydrothermal melamine treatment for 24 h at 180 °C, followed by calcination at 550 °C for 4 h. In the case of MD, the material appears to be smoother than MH, yet no morphological control is observed either.

The images of the MHB and MHWB heterojunctions show aggregates of globular particles surrounded by smooth structures. A similar aspect is observed for the MDB and MDWB samples; however, for these samples, the spherical particles are bigger and appear surrounded by a smooth and low conductive structure. Thus, the hypothesis is that the presence of MD and MH in the reaction medium affects the adsorption capacity of species on the $BiVO_4$ surface. For this reason, the PVP polymeric layer does not accumulate on $BiVO_4$; thus, the particles and W-$BiVO_4$ cannot self-organize into larger squares. Therefore, we can assume that MD and MH interact physically or chemically with the surface of (W)-$BiVO_4$.

Fig. 2 shows TEM images of the MHB, MDB, MHWB and MDWB samples. The images show regions of high contrast formed by globular

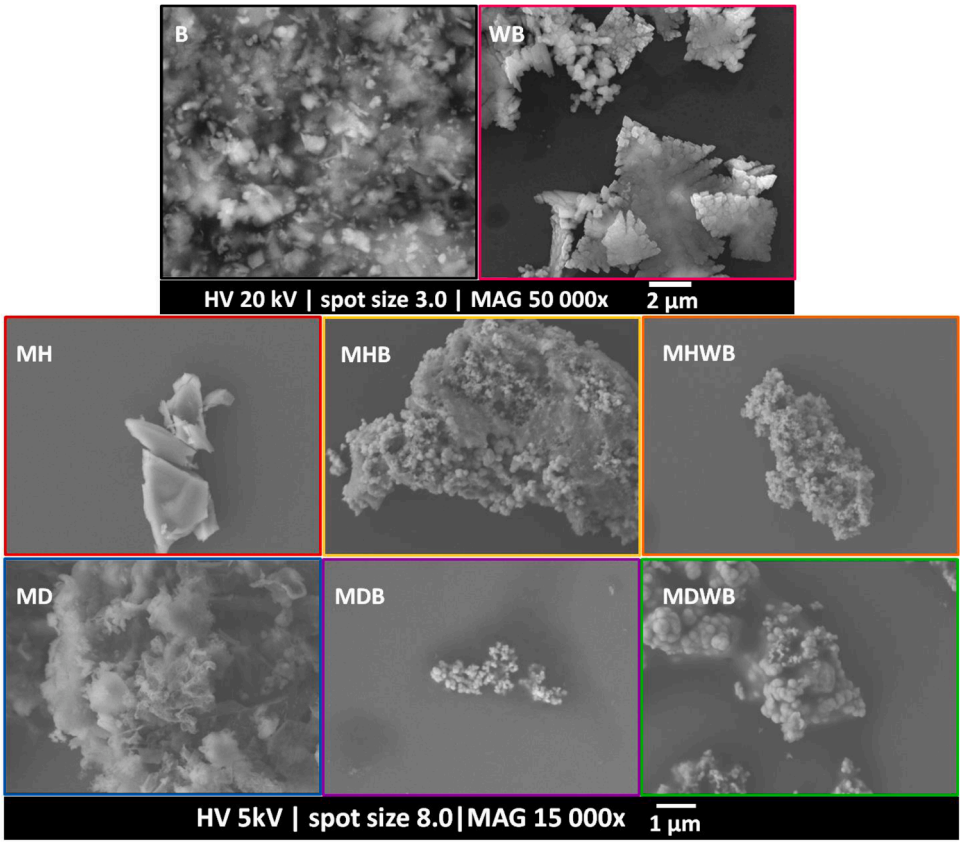

Fig. 1. Scanning electron microscopy images of the B, WB [26], MH, MHB, MHWB, MD, MDB and MDWB samples.

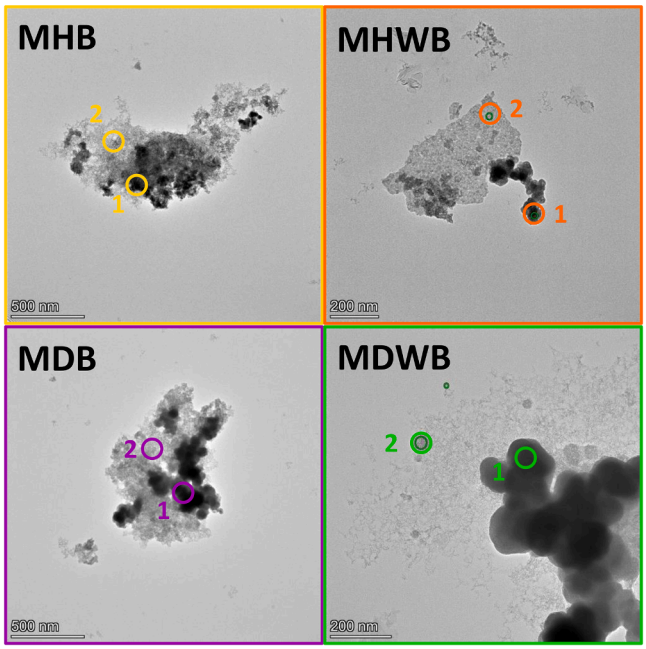

Fig. 2. Transmission electron microscopy images of the MH, MHB, MHWB, MD, MDB and MDWB samples.

particles and areas of lower contrast containing a mass of particles with no controlled morphology. EDS mapping (Figures S1–4) shows that the regions containing globular particles (1) are rich in Bi and V, while species with a higher proportion of carbon form the lower contrast regions (2). This result reinforces the hypothesis raised by the SEM images. It is important to note that detecting W in the MHWB and MDWB samples by EDS analyses was impossible, probably due to its low concentration.

XRD diffractograms (Fig. 3) were collected to understand the resultant crystalline structures. The synthesized samples show the same diffraction pattern, with a single characteristic peak at approximately 27.5°. This peak can be attributed to the (002) plane of the layered stacking of C_3N_4 [17], which can be formed by the interplanar stacking of aromatic systems [5]. Monoclinic $BiVO_4$ can also be associated with the peak around 28° assigned to the (121) plane (ICSD 391,414). In the literature, it is reported that the (121) peak of $BiVO_4$ eventually shifts to the left with increasing doping with C_3N_4 due to its strong interaction [5, 7]. Thus, the observed peak may have contributions of both $BiVO_4$ and C_3N_4, which may increase its intensity [28]. Alternatively, the suppression of other characteristic peaks of $BiVO_4$ may have occurred due to the large amount of C_3N_4 that generated a layered stacking on the $BiVO_4$ surfaces.

Raman spectra were collected to confirm the presence of $BiVO_4$ in the samples. Fig. 4a shows the Raman spectra of B and WB. The monoclinic structure of $BiVO_4$ is confirmed by observing bands located at 211, 327, 369, 710 and 828 cm^{-1} [29]. These spectra are dominated by an intense band near 810–820 cm^{-1}, attributed to the V-O symmetric stretching mode [29–30]. Two bands at 369 and 330 cm^{-1} correspond to the symmetric and asymmetric bending modes of the VO_4 tetrahedra, respectively [30]. An intense band was observed for both spectra around 752 cm^{-1}, which can be attributed to V-O's $\nu 3$ asymmetric stretching mode (VO_4^{3-}) [31]. Tungsten doping for material causes a decrease in the intensity of the bismuth vanadate bands. Fig. 4b shows the Raman spectra of MD and MH. A band is observed around 700 cm^{-1}, originating from the vibration modes of the CN heterocycles in g-C_3N_4 [32]. Broadband between 1400 and 1530 cm^{-1} can also be observed when there is a symmetrical stretching of trigonal C—N(-C)-C or C—NH—C bridging units, commonly designated by the D and G bands [33]. At approximately 1500 cm^{-1}, a peak can be associated with a typical

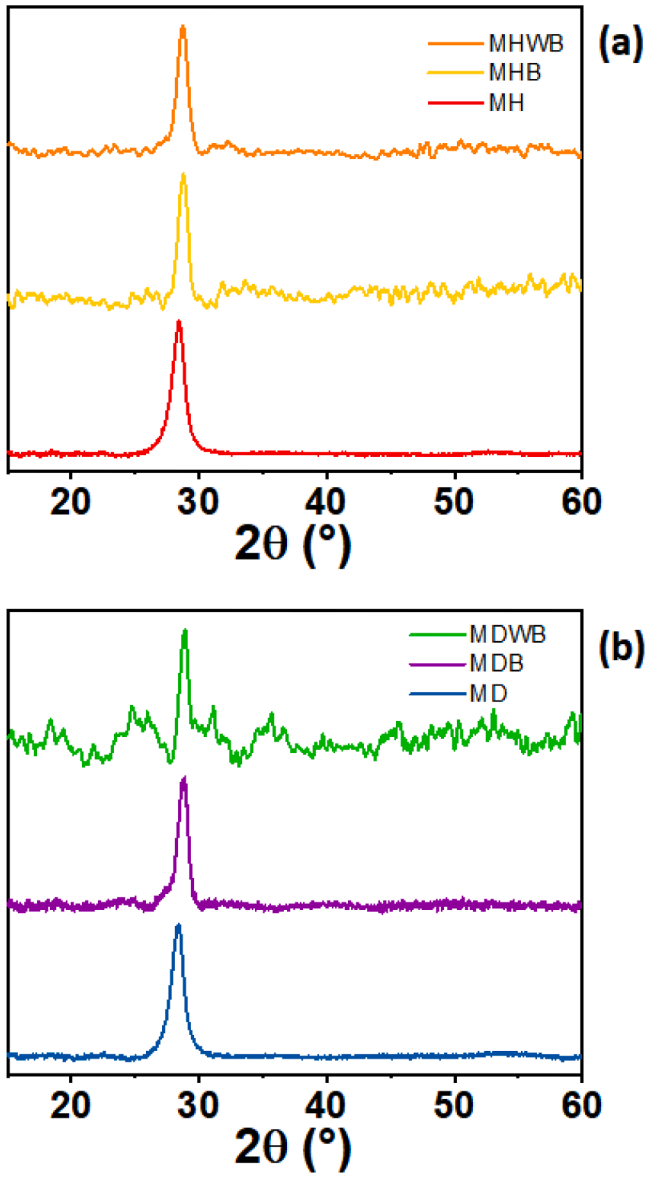

Fig. 3. X-ray diffractograms of the materials (a) MHWB, MHB, MH and (b) MDWB, MDB, MD collected by D8 Focus diffractometer (Bruker) Cu Kα radiation source operating at 40 kV and 40 mA.

graphite structure's D and G bands [32]. At 1530 cm^{-1}, it comes from the $-NH_2$ bending modes present in the structure of the material [34]. These peaks confirm the formation of C_3N_4 in the materials.

The Raman spectra of MHB and MDB materials (Fig. 4c) show a combination of the bands ascribed to the monoclinic $BiVO_4$ monoclinic and C_3N_4. Finally, Raman spectra of MHWB and MDWB (Fig. 4d) also show the peaks ascribed to the monoclinic $BiVO_4$ and C_3N_4. However, a peak at approximately 300 cm-1 related to the deformation of the W-O-W bond 41–43 is observed for the tungsten-doped samples. There is an increase in the peak intensity at 810 cm^{-1}, which is also characteristic of WO_3 nanocrystals in their monoclinic and orthorhombic forms [35–37].

Fig. 5a shows the UV–Vis spectra of the obtained samples. All samples exhibit broad absorption bands in the 400 to 700 spectral interval. MD and MH absorption is more intense between 400 and 450 nm. The composites MDB and MHB show an intensification of the light absorption around 500 nm 500 nm due to the incorporation of the g-C_3N_4. The W-doped samples also increase the absorption in the 450–500 nm range, indicating that the tungsten ions play a role in the light absorption, probably via charge transfer mechanisms. The band gap energy of the

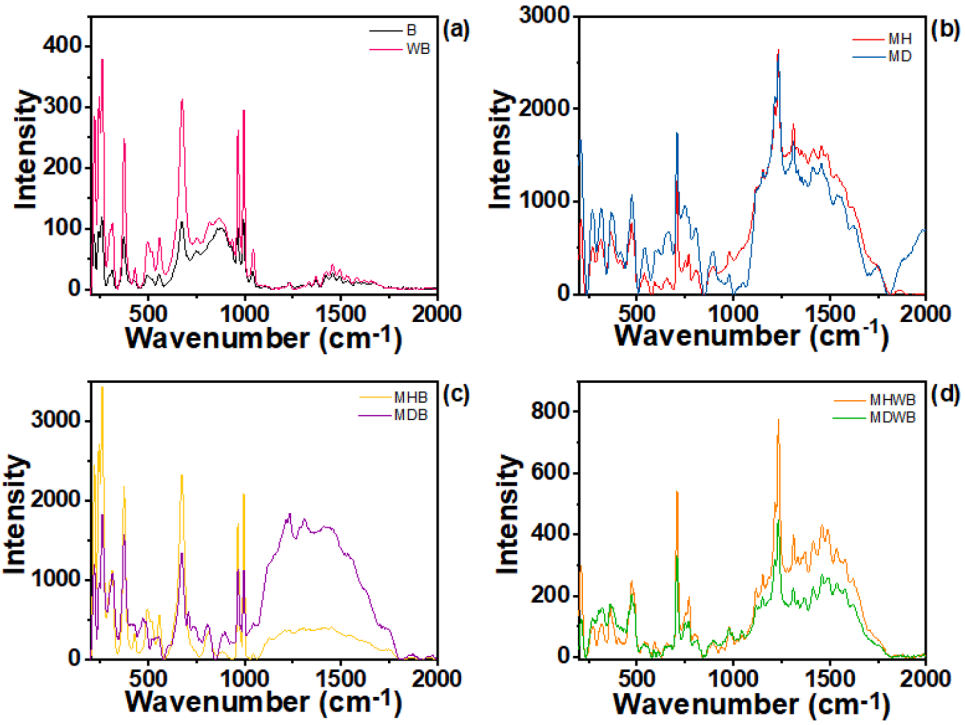

Fig. 4. Raman spectra of the materials (a) B and WB, (b) MH and MD, (c) MHB and MDB, (d) MHWB and MDWB collected in a labRam HR Evolution (HORIBA) spectrometer using a 785 nm laser.

materials was estimated by analyzing the diffuse reflectance spectrum in the UV–Vis region. The Tauc-plot method was used to calculate the band gap energies, Eq. (1) [38].

$$(\alpha h\nu)^{1/2} = A(h\nu - E_g) \quad (1)$$

where $\boldsymbol{\alpha}$ is the optical absorption coefficient, $\boldsymbol{h\nu}$ is the photon energy, $\boldsymbol{E_g}$ is the transition energy, and $\boldsymbol{A}$ is a proportionality constant. In the method described by Tauc, a linear fit is applied to the peak of the steepest slope represented in the graphs by the red dotted line (Fitted line). In addition, a linear fit is applied using the abscissa axis defined in the graph by the blue dotted line (baseline). The two lines are then intersected to estimate the band gap energy shown for the MH material in Fig. 5b [38]. Tauc plot treatment for the other materials is exhibited in Figure S5.

Table 1 summarizes the band gap energies calculated for the materials. The values are between 2.30–2.83 eV, where the MDB sample exhibits the highest energy and MDWB the lowest. However, it can be seen that most of the values were between 2.7 and 2.8, which is according to the literature, as g-C_3N_4 has a band gap between 2.7 −2.8 eV even when varying the starting reagent used to synthesize it [39,40]. Meanwhile, $BiVO_4$ has a band gap energy of around 2.4 eV [39,41], which may have influenced the decrease in the band gap energy of the MDWB material.

The zeta potential values of MH and MD vary from positive to negative upon increasing the pH (Figure S6 and Table S1). The zeta potential values of MD show a more significant variation (from +15.9 to −15.0 mV), whereas the values found for MH vary from +0.50 to −6.1 mV. According to the literature, the zeta potential of g-C_3N_4 can range from 0.91 to −27 mV, depending on the precursor used for the synthesis and the synthesis method [42–46]. For instance, at the same pH, g-C_3N_4 produced from melamine, thiourea and urea showed a potential of −17.0, −30.7 mV and −19.9 mV, respectively [46]. The same precursor has been used; however, the synthesis method has changed. For the synthesis of MH, melamine was subjected to a hydrothermal treatment before the annealing process; conversely, the MD was produced by the direct calcination of melamine. Thus, we can conclude that the variation of zeta potentials results from the different synthesis protocols used. The smooth surface of MD (see SEM images Fig. 1) may result in a higher amount of -NH groups available at the surface responsible for the changes of the zeta potential as a function of pH when compared to MH, which has a more compact morphology.

The MHB and MDB zeta potentials became more negative (Figure S6 and Table S1). This result is consistent with the literature since the zeta potential of $BiVO_4$ can range from −5.21 to −53 mV [47-49], while the value found for $BiVO_4$ modified with g-C_3N_4 is −35.5 mV at pH 6 [14,20,21,23,24,50,51,52,53,17,54,25,55,18,56,57]. Finally, it was found that the zeta potential became slightly more positive for MDWB. For the MHWB, the values are like those of the MHB. These results agree with those previously reported by our group [49].

The FTIR spectra of the samples are shown in Fig. 6. It can be observed that all samples exhibit the same pattern with differences in the peak intensities. The broad band at around 3000–3400 cm^{-1} is characteristic of the six vibrations of the structure of melamine, which presents 3 NH_2 groups and 6 N—H bonds; these bonds can be superimposed on each other to produce two bands at 3414 cm^{-1} and 3477 cm^{-1} [58,59,60]. These peaks can also be ascribed to non-condensed amino functional groups in g-C_3N_4 prepared by melamine at 3130 cm^{-1} and 3327 cm^{-1} [58,59,60]. The peak at 3400 cm^{-1} is also ascribed to the stretching vibrations of the O—H group, which may come from adsorbed water molecules [61]. There is also a contribution from C–H asymmetric stretching vibrations peaked at 3135 and 2929 cm^{-1}[62].

In addition, an overlap of peaks was observed in the range between 500 and 2000 cm^{-1}, ascribed to the interactions of the compounds involved in the synthesized materials. For better visualization, Figure 6 (a) shows the FTIR spectrum ranging from 1800 to 500 cm^{-1} of the MHWB material as an example.

The peak at 1640 cm^{-1} (a) can be assigned to the C—N stretching of tri-s-triazine [58,59,60]. It is observed at approximately 1560–1200 cm^{-1} (b-e) bands, which are characteristic of the symmetric stretching of the C = N bond [58,59,60,63,64]. At 700–1100 cm^{-1} (f-i), bands are associated with the vibration of the tri-s-triazine ring [58,59,60,63,64].

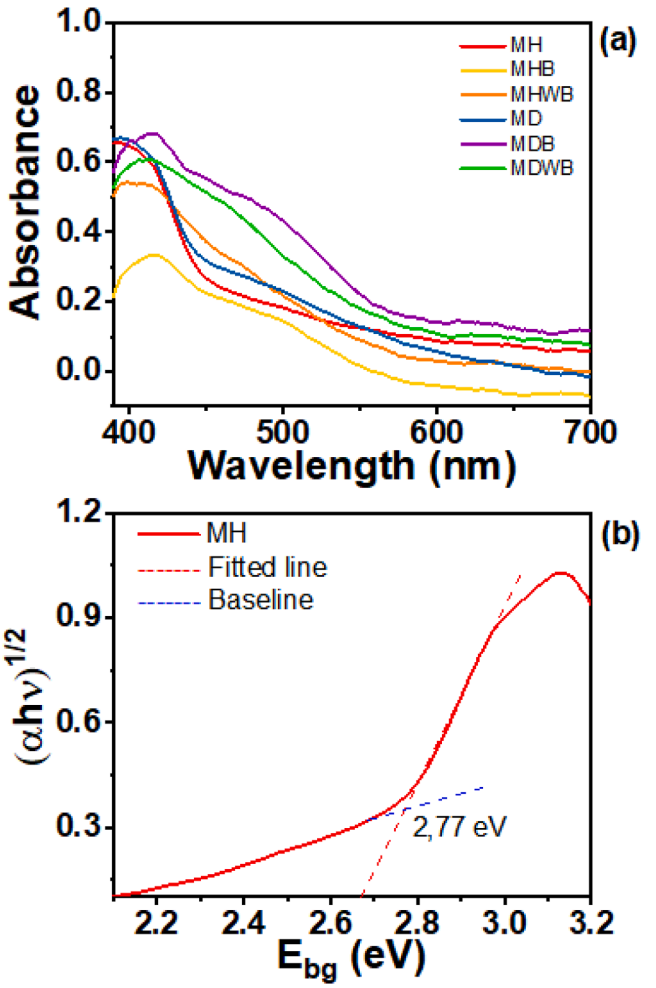

Fig. 5. (a) Reflectance graph with Tauc plot and (b) Reflectance graph using the Tauc indirect electron injection method for the MH.

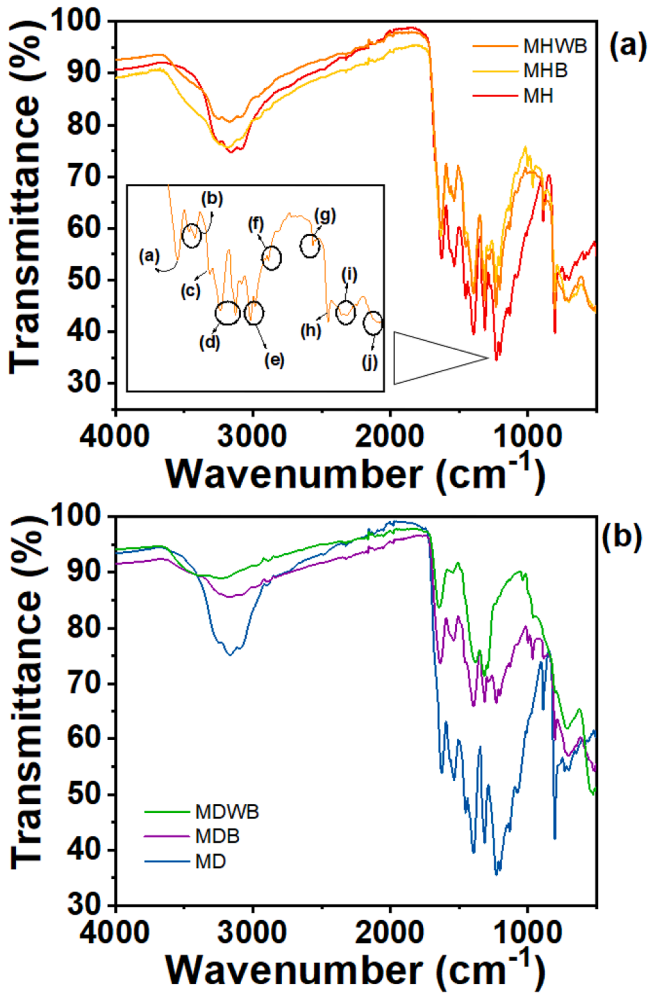

Fig. 6. Fourier-transform infrared spectroscopy for the materials (a) MHWB, MHB, MH and (b) MDWB, MDB, MD.

Table 1
Band gap energy of the materials MH, MHB, MHWB, MD, MDB and MDWB.

Material	Band gap (eV)
MH	2.77
MHB	2.78
MHWB	2.73
MD	2.82
MDB	2.83
MDWB	2.30

Finally, around 550 cm^{-1} (j), a band is observed that can be related to the bending of the C_3N_4 ring [58,59,60,63,64]. The MHB, MHWB, MDB, and MDWB samples also show the band at 700–1100 cm^{-1} (f-i) characteristic of the symmetric and asymmetric stretching of the bonds $n_1(VO_4)$ and $n_3(VO_4)$ [61,65]. In addition, the band at approx. 640 cm^{-1} (i) can be ascribed to Bi-O bending [61].

The presence of PVP can also be proved by the observation of the bands at 1647 cm^{-1}(a), 1225 cm^{-1} (e) and 1084 cm^{-1} (f) to the C—O stretching [66]. As previously described, these bands overlap with C—N stretching [66]. An increased bandwidth in (b) may be because of the C—H group (alkane groups) [66]. Finally, the tungsten (W) present in MHWB and MDWB may result in an extra band around 900–1100 (f) corresponding stretching of the $W = O$ bonds at the surface [67]

Fig. 7 shows that the MHB, MHWB, MDB and MDWB materials have good thermal stability, with approximately 20 % mass loss even at 400 °C. For the MH and MD materials, different mass loss profiles were observed as a function of temperature. A constant mass loss is observed for MD from 250 °C onwards, reaching 100% degradation at around 320

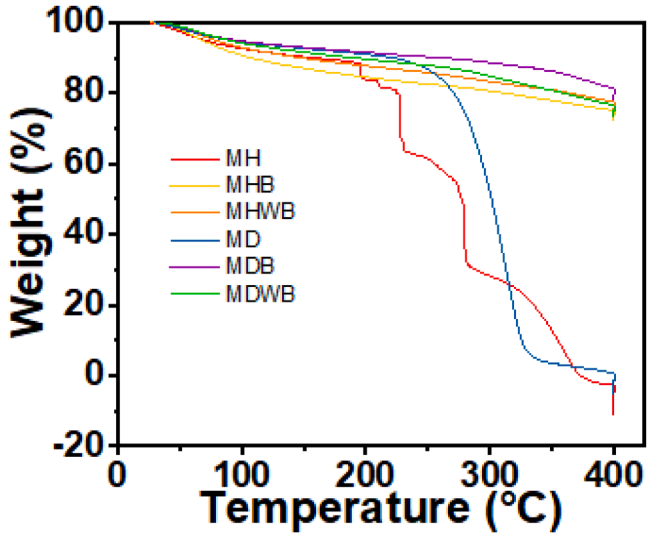

Fig. 7. TGA curve in the presence of nitrogen and heating speed of 10 °C min^{-1} for MH, MHB, MHWB, MD, MDB and MDWB.

°C. For MH, its profile shows different moments that may indicate losses of volatiles from 200 °C, and mass varies sharply until it reaches 400 °C. These results support the idea that heterojunction with bismuth vanadate helps to enhance the thermal stability of the materials.

3.2. Photoelectrochemistry

Chopped-light chronoamperometry (Fig. 8a, b, c) was used to measure the photocurrent density generated during water oxidation as simulated solar light was irradiated on the front side of the film. This is an important measure, as the photocurrent is directly proportional to the efficiency of electron-hole separation [68].

The fast response to the light of the materials studied can be verified because they have a constant photocurrent when the light is on and decrease rapidly to zero almost immediately when the lamp is turned off [23,69]. The only exception is the MH, which exhibits a slow photoresponse. One explanation for this behavior could be the significant trapping of photogenerated electrons in deep trap states, giving rise to long-lived trapped electrons that are slow to respond when illuminated [70].

Fig. 8a shows the chronoamperometry results of the pristine $BiVO_4$ (B) and $WBiVO_4$ (WB). Doping with tungsten increased the photocurrent measured, indicating lower recombination. Fig. 8b shows that the photocurrent generated increases in the following order: MHB< MH< MHWB. On the other hand, the photocurrent increases in the following order for the materials based on MD: MDWB<MD<MDB (Fig. 8c). Thus, the heterojunctions MHWB and MDB show greater efficiency in separating electrons and holes, which reduces the recombination of photogenerated charges. The MHWB material showed consistency with the result found in Fig. 8a, where doping with tungsten improved the photocurrent of the material. In the literature, the heterojunction between g-C_3N_4 and $BiVO_4$ is very efficient since the formed interface promotes faster interfacial charge transfer, as well as greater separation between electrons and holes, which are the main reasons for its improved photocatalytic activity [23,68,71]. The fact that MHB exhibits lower activity than MH can be due to the formation of an intermediate species at the interface that does not allow a favorable charge transfer. The same happened for the MDWB material (Fig. 8c). For the MHWB, on the other hand, this increase in photogenerated charges works favorably. Thus, the hydrothermal treatment plays a critical role in the species formed at the interface of each heterojunction. Xu and collaborators [72] reported a heterojunction formed between 2D g-C_3N_4 and $BiVO_4$

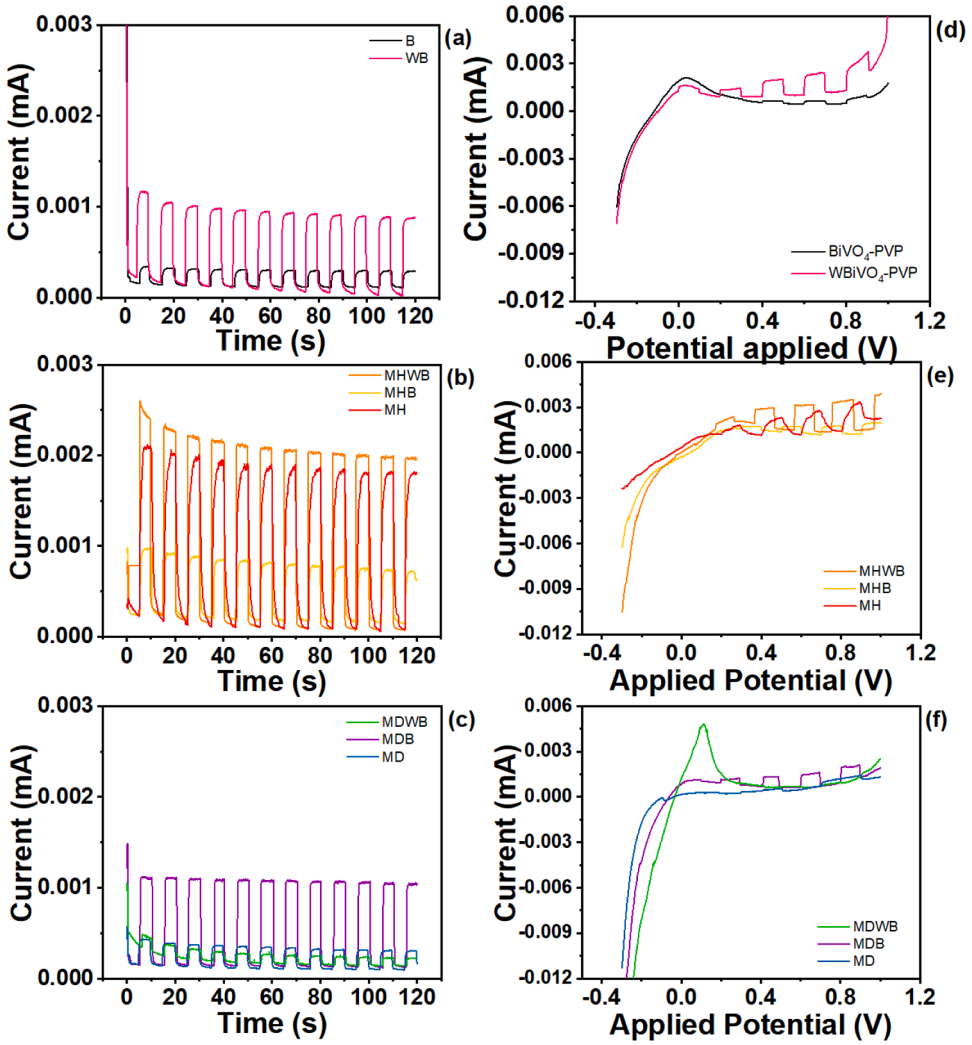

Fig. 8. (a) Chopped-light chronoamperometry experiments using B and WB films as working electrodes (b) Chopped-light chronoamperometry experiments using MH, MHB, and MHWB films as working electrodes (c) Chopped-light chronoamperometry experiments using MD, MDB, and MDWB films as working electrodes. (d) Chopped-light linear sweep voltammetry using B and WB films as working electrodes (e) Chopped-light linear sweep voltammetry using MH, MHB and MHWB films as working electrodes. (f) Chopped-light linear sweep voltammetry using MD, MDB and MDWB films as working electrodes. Counter electrode: Pt; Reference electrode: Ag/AgCl; Electrolyte 0.1 M Na_2SO_4 aqueous solution (b,c,e,f) and 0.1 M Na_2SO_4 10 % buffer pH 7 (a,d). Applied bias 0.8 V in Chopped-light chronoamperometry and 0.3–1 V in Chopped-light linear sweep voltammetry.

and found lower photocurrents than those reported here; however, the electrode preparation or photoelectrochemical experimental conditions are different. Therefore, we tested commercial P25 under the same experimental conditions (Fig. S9) and found that MH and MHWB showed higher photocurrents during the chronoamperometry experiments.

The linear scan measurement (Fig. 8d, e, f) was carried out to verify the photocurrent response of the synthesized materials, where it was possible to see that WB, MH, MHB, MHWB and MDB showed an excellent response to light. As can be seen, MHWB was the material with the highest photocurrent efficiency among all investigated ones.

Firstly, in Fig. 8e, we see that the onset potential of the B material is around 0.2 V, while for the WB material, it is around 0 V. Fig. 8e shows that the onset potential of MH is about 0.3 V, whereas MHB is 0.2 V and MHWB is 0.0 V. This result indicates that doping the $BiVO_4$ with tungsten reduces the potential required for water oxidation. MD showed an onset potential close to 0.2 V (Fig. 8f). In contrast, MDB showed an onset of around 0.1 V. Following the low photoactivity observed in the chronoamperometry experiments, the MDWB does not show photoresponse upon the linear sweep voltammetry. This material exhibits a less crystalline XRD pattern, which could suggest that the crystalline connection between the composite components does not favor the charge transfer process.

Electrochemistry measurements were also carried out by controlling the pH at 7 using a buffer solution (Fig. S7). However, the photocurrents are lower than those obtained without pH control (Fig. 8). Only MHB material showed better results even under a low bias of 0.2 V in pH 7. This result indicates that pH control favors bismuth vanadate in the heterojunction with graphitic carbon nitride. Still, when doped with tungsten, it does not show the best results compared to when pH control is not applied.

IPCE measurements were performed under open circuit conditions (Fig. 9a). The results can be expressed from Eq. (2), i.e., as a function of the electron injection quantum efficiency Φ_{EI}, the electron collection efficiency in the external circuit, η_{EC} and the light-harvesting efficiency, LHE, at a given wavelength [73].

$$\mathrm{IPCE}(\lambda)\ \Phi_{EI}\ .\ \eta_{EC}\ .\ \mathrm{LHE} \tag{2}$$

As seen in Fig. 9, the IPCE results showed a maximum value of around 33 % for the $BiVO_4$ and MHB materials at 400 nm, and these two materials also showed the best results over the wavelengths swept from 400 nm to 700 nm. The IPCE results differ from those observed in the photoelectrochemistry experiments because they were carried out in an open circuit. Thus, $BiVO_4$ and MHB showed interesting results since they showed good photocatalytic response under visible light.

Fig. 9b shows the photoluminescence of all materials reported here. The emission spectra of the g-C_3N_4 show a broad band from ca. 425 to 600 nm, with a maximum of 458 (MD) and 468 nm (MH). The emission is assigned to the optical band gap related to the sp^2 clusters [74]. The shift of the emission peak of the g-C_3N_4 can be attributed to the method of preparation that induces the condensation of the melamine at different temperatures. The hydrothermally treated material contains adsorbed solvents and volatile species that can alter the temperature of condensation, leading to different optical band gaps.

The emission spectrum of the $BiVO_4$ material is composed of a broad band with a maximum of 445 nm (2.78 eV) assigned to the band-to-band transition. The W-doping promotes a drastic emission quenching, indicating a slow e^--h^+ recombination process. The doping process usually creates energy levels within the band gap that activate different energy relaxation pathways. The quenching in the emission band of the W-doped samples is consistent with the increase in the anode photoresponse since the radiative recombination competes with the observed photocurrent; if the generated photocarrier suffers radiative recombination, it is no longer available to generate photocurrent in the circuit.

The combination of the MH and $BiVO_4$ in a composite yields a very intense emission band centered at 463 nm, consistent with the optical band gap transition of g-C_3N_4. Similarly, the W-doping leads to a drastic quenching of the emission band, as discussed above.

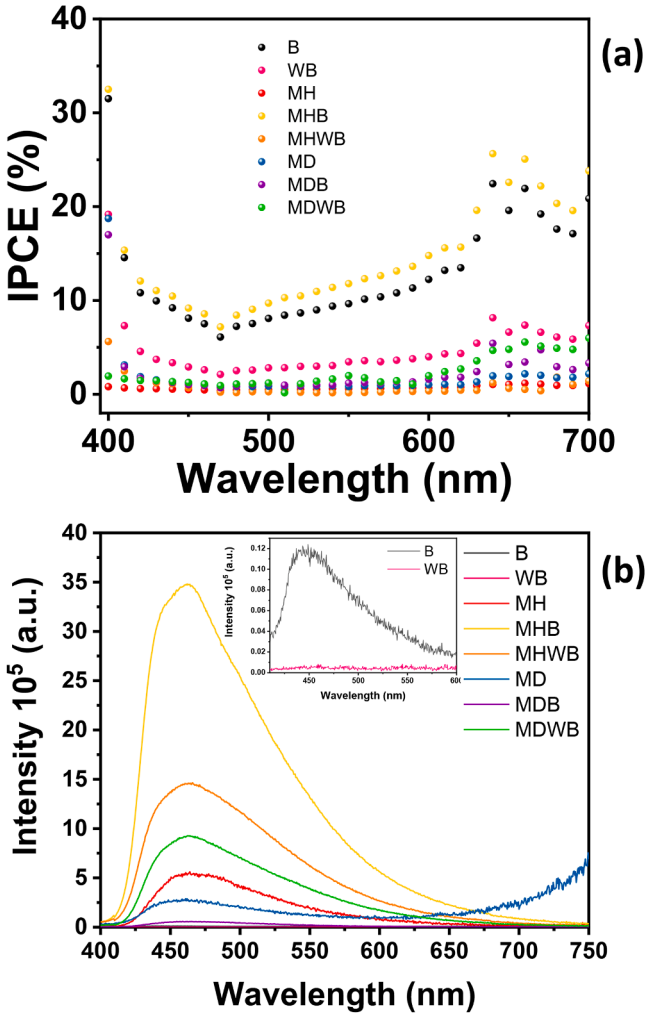

Fig. 9. (a) IPCE as a function of the electron injection quantum efficiency Φ_{EI}, the electron collection efficiency in the external circuit, η_{EC} and the light-harvesting efficiency, LHE, at a given wavelength for the materials B, WB, MH, MHB, MHWB, MD, MDB and MDWB films as working electrodes. Counter electrode: Pt; Electrolyte 0.1 M Na2SO4 10 % buffer solution pH 7. (b) Photoluminescence spectra of the investigated materials.

The composites prepared with MD and $BiVO_4$ show a reversed behavior, where the W-doping increases the emission intensity. The results corroborate the decrease in the photocurrent generation. The results indicate that the MH generates a well-aligned energy band that optimizes the photocurrent generation.

3.3. Photocatalysis

Tetracycline (TC) was used as an organic model to evaluate the photocatalytic activity of the materials reported here. It is a widely used antibiotic to treat bacteria-related diseases in humans and animals; however, it is completely metabolized by humans or animals. Therefore, a significant fraction is excreted and accumulates in aquatic environments [72,75]. Thus, developing a method to eliminate such residues from wastewater is critical. Fig. 10 shows the TC degradation rate using B and WB (Fig. 10a); MH, MHB and MHWB (Fig. 10b); MD, MDB and MDWB (Fig. 10c) and P25 (Fig. 10d) as photocatalysts under simulated sunlight irradiation. It can be observed that after 1 h of sunlight exposure, B is more active than WB (Fig. 10a); this result is opposite to the trend observed for the photocurrent measurements. A possible

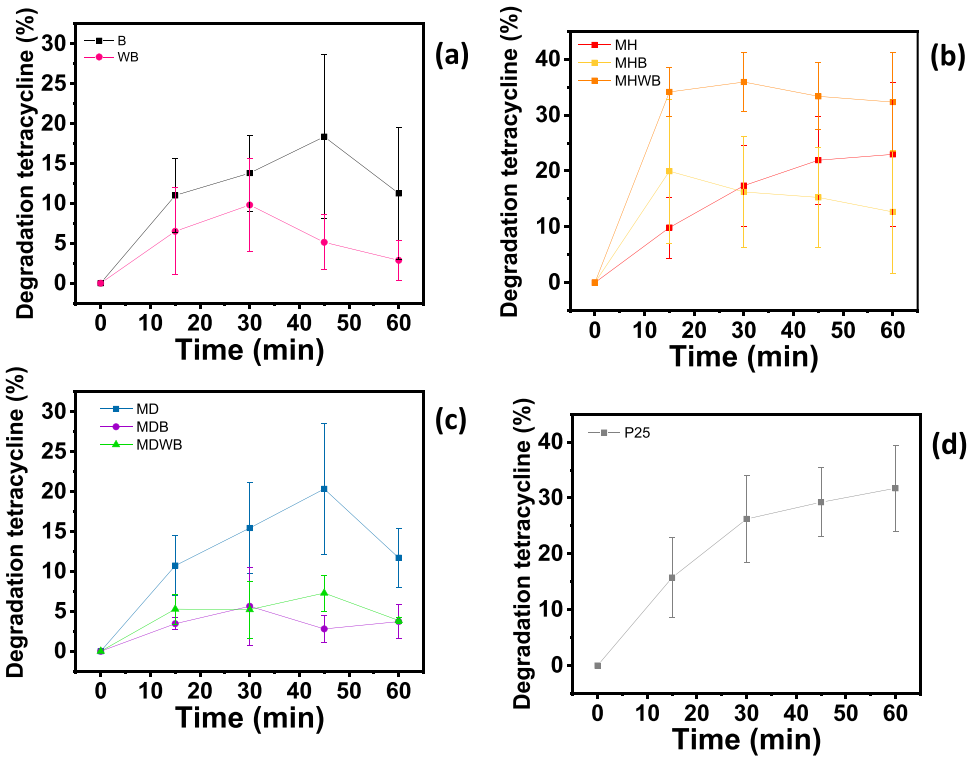

Fig. 10. Tetracycline photodegradation using the following catalysts: B and WB (a); MH, MHB and MHWB; MD, MDB and MDWB (c); and P25 (d).

explanation is the higher IPCE values observed for B (Fig. 9a), which can be associated with its charge separation capacity. Also, the differences in the surface compositions of B and WB may induce different chemical interactions with the TC since changes in the appearance of the UV–vis spectra (Figures S11 and S12) suggest an instability of the molecular structure during the adsorption process [76]. For the MH, MHB and MHWB materials, the dye degradation efficiency after 1 h of simulated sunlight irradiation follows the same trend as that observed for the photocurrents (Fig. 8b), which can be ascribed to a suitable band alignment as suggested by the photoluminescence study. Also, the UV–Vis spectra suggest different interactions of each catalyst with the TC (Figures S13–15). Finally, MD shows higher photoactivity than MDB and MDWB (Fig. 10c), which does not match the trend of photocurrent generation (Fig. 8c). Also, it can be explained by a unique interaction of TC with MD since the UV–Vis spectra of the supernatant are very different from those observed when MDB and MDWB are used as photocatalysts (Figures S16–18).

Among all investigated materials, MHWB had the highest photocatalytic activity. We are unaware that another study has been reported involving heterojunctions between W-doped $BiVO_4$ and g-C_3N_4 for tetracycline photodegradation. However, Kang and coworkers [77] have prepared Na^+- doped $BiVO_4$ and g-C_3N_4 heterojunction and applied it to TC degradation using a 300 W Xenon lamp equipped with a UV cut-off filter (< 420 nm), which showed 60 % efficiency after 40 min of irradiation. Xu and collaborators [72] reported a heterojunction between 2D g-C_3N_4 and $BiVO_4$. They found a photocatalytic activity towards TC degradation of ~65 % after 1 h of irradiation of a 500 W Xe lamp with a cut-off filter ($\lambda \geq 420$ nm). Although these two studies reported higher activities than the one found in this work, it is essential to highlight that the irradiation power used here is much lower. Thus, to better compare our results with the literature, we submitted commercial P25 to the same photocatalytic conditions and found that the efficiency of MHWB was very similar to that of P25. However, the maximum degradation rate is reached faster for MHWB than P25. These results reinforce how the hydrothermal treatment of melamine before the calcination to produce g-C_3N_4, combined with the W-doping of $BiVO_4$, are successful strategies to improve the photocatalytic activity of the heterojunction.

4. Conclusions

In conclusion, this study systematically examined the morphological characteristics, crystalline structures, and photocatalytic performances of heterojunctions involving $BiVO_4$ and W-$BiVO_4$ with graphitic carbon nitride (g-C_3N_4) produced through distinct synthesis routes. The first method involved submitting melamine to a hydrothermal treatment before the annealing process (MH); the second involved the direct annealing of melamine (MD).

SEM images revealed that MD shows an irregular shape with sharp edges, whereas the MD exhibits an irregular and very smooth shape. Thus, the hydrothermal treatment affected the way g-C_3N_4 aggregates. Images of pristine $BiVO_4$ and W-$BiVO_4$ show irregular and square shapes, respectively. The combination of $BiVO_4$ and W-$BiVO_4$ with MH and MD shows that none of the pristine morphologies was retained during the synthesis of the heterojunction. This observation suggests (i) that there is an interaction between (W)-$BiVO_4$ and g-C_3N_4 and (ii) that the g-C_3N_4 and (W)-$BiVO_4$ are homogenously distributed onto each other.

Photoelectrochemical experiments show that doping $BiVO_4$ with tungsten enhances the photoresponse of the anode three times. This result is expected since it is recognized from the literature that the insertion of W into the $BiVO_4$ reduces the recombination sites. Combining W-$BiVO_4$ with MH increases the photocurrent 3.3 times (compared to pristine W-$BiVO_4$). On the other hand, the photocurrent obtained using the system MHB (MH and $BiVO_4$) is two times higher than $BiVO_4$ but two times lower than pristine MH. Conversely, when MD is used, the photocurrent of MDB (MD and $BiVO_4$) is almost four times higher than MDWB (MD and W-$BiVO_4$). Another interesting observation is that the photocurrent obtained by MH is five times higher than that obtained by MD. However, the photoresponse of MD is faster than MH, which exhibits deep trap states.

Photodegradation tests reveal that the synthesis methods may affect the surface of the photocatalysts and, as a result, the adsorption of

tetracycline (organic model). Still, MHWB was the best photocatalyst, degrading 40 % of TC after 1 h of simulated sunlight irradiation, which was comparable to the activity of commercial P25 tested under the same conditions (Figs. 10d and S19).

These results suggest that the hydrothermal treatment influences the structure and surface characteristics of g-C_3N_4, affecting how the material aggregates and interacts with $BiVO_4$ and W-$BiVO_4$. The MH promotes a heterojunction that enhances the charge processes with W-$BiVO_4$. On the other hand, the MD results in a more favorable heterojunction with $BiVO_4$. However, overall, higher currents were obtained when MH was used.

Thus, we can conclude that introducing a hydrothermal treatment of melamine before the calcination step resulted in the formation of heterojunctions with W-$BiVO_4$, resulting in photoanodes with enhanced response.

CRediT authorship contribution statement

Caroline H. Claudino: Writing – original draft, Methodology, Investigation, Formal analysis, Data curation. **Marcos R.S. Vicente:** Formal analysis, Data curation. **Maria Kuznetsova:** Formal analysis. **José M. De Carvalho:** Formal analysis, Investigation, Methodology. **Juliana S Souza:** Writing – original draft, Validation, Supervision, Resources, Project administration, Methodology, Funding acquisition, Data curation, Conceptualization.

Declaration of competing interest

The authors declare that they have no known competing financial interests or personal relationships that could have appeared to influence the work reported in this paper.

Data availability

Data will be made available on request.

Acknowledgments

This work was supported by FAPESP (grants 2021/05958-4, 2020/02886-0 and 2023/14930-1). This study was also financed in part by the Coordenação de Aperfeiçoamento de Pessoal de Nível Superior – Brasil (CAPES) – Finance Code 001 and 88887.920560/2023-00. The authors also acknowledge Conselho Nacional de Desenvolvimento Científico e Tecnológico (CNPq). Finally, we thank LNNano-CNPEM for using the SEM facility and the Multi-users platform (CEM) at UFABC for instrumental facilities.

Supplementary materials

Supplementary material associated with this article can be found, in the online version, at doi:10.1016/j.materresbull.2024.112955.

References

[1] X. Sun, S. Jiang, H. Huang, H. Li, B. Jia, T. Ma, Angew. Chem. 61 (2022) e202204880.
[2] M. Benghanem, A. Mellit, H. Almohamadi, S. Haddad, N. Chettibi, A.M. Alanazi, D. Dasalla, A. Alzahrani, Energies 16 (2023) 757.
[3] C. Hu, M. Tian, L. Wu, L.J.E. Chen, Ecotoxicol Environ Saf. 231 (2022) 113175.
[4] Z. Chen, Y. Li, F. Tian, X. Chen, Z. Wu, Sep. Purif. Technol. 287 (2022) 120507.
[5] S. Dong, G.J. Lee, R. Zhou, J.J. Wu, Sep. Purif. Technol. 250 (2020) 117202.
[6] Z. Li, C. Jin, M. Wang, J. Kang, Z. Wu, D. Yang, T. Zhu, Sep. Purif. Technol. 232 (2020) 115937.
[7] K. Zhong, J. Feng, H. Gao, Y. Zhang, K. Lai, J. Solid. State Chem. 274 (2019) 142.
[8] B. Zhang, H. Zhang, Z. Wang, X. Zhang, X. Qin, Y. Dai, Y. Liu, P. Wang, Y. Li, B. Huang, Appl. Catal. B: Environ. 211 (2017) 258.
[9] L. Wu, M. Wang, T. Han, B. Yang, L. Geng, J. Jin, J. Alloys. Compd. 949 (2023) 169822.
[10] Y. Shuai, R. Peng, Y. He, X. Liu, X. Wang, W. Guo, Sens. Actuat. B: Chem. 384 (2023) 133625.
[11] M. Liaqat, N.R. Khalid, M.B. Tahir, S. Znaidia, H. Alrobei, M. Alzaid, Ceram. Int. 49 (2023) 10455.
[12] L. Li, M. Mao, X. She, J. Yi, M. He, L. Pan, Z. Chen, H. Xu, H. Li, Mater. Chem. Phys. 241 (2020) 122308.
[13] W. li Zhao, Y. hua Gao, D. Zhang, Chem. Phys. Lett. 787 (2022) 139268.
[14] F. Guo, W. Shi, X. Lin, G. Che, J. Phys. Chem. Solids 75 (2014) 1217.
[15] J. Wang, X. Lian, S. Chen, H. Li, K. Xu, J. Colloid Interface Sci. 610 (2022) 842.
[16] M. Kocijan, M. Vukšić, M. Kurtjak, L. Ćurković, D. Vengust, M. Podlogar, Catalysts 12 (2022) 1554.
[17] T. Ahmed, M. Ammar, A. Saleem, H.-l. Zhang, H.-b. Xu, RSC. Adv. 10 (2020) 3192.
[18] Z. Jin, Y. Zhang, D. Liu, H. Ding, B.B. Mamba, A.T. Kuvarega, J. Gui, Sep. Purif. Technol. 277 (2021) 119224.
[19] V. Jayaraman, C. Ayappan, A. Mani, Chemosphere 287 (2022) 132055.
[20] M. Song, Y. Wu, C. Du, Y. Su, J. Colloid. Interface Sci. 588 (2021) 357.
[21] M. Song, Y. Wu, G. Zheng, C. Du, Y. Su, Appl. Surf. Sci. 498 (2019) 143808.
[22] K. Zhang, L. Wang, Y. Hong, X. Duan, C. Ai, L. Zhang, T. Zhang, Y. Chen, X. Lin, W. Shi, J. Alloys Compd. 966 (2023) 171580.
[23] Y. Wang, G. Tan, T. Liu, Y. Su, H. Ren, X. Zhang, A. Xia, L. Lv, Y. Liu, Appl. Catal. B: Environ. 234 (2018) 37.
[24] H.J. Kong, D.H. Won, J. Kim, S.I. Woo, Chem. Mater. 28 (2016) 1318.
[25] W.-K. Jo, T.S. Natarajan, J. Colloid. Interface Sci. 482 (2016) 58.
[26] B.S. Rodrigues, C.M. Branco, L.R.M. Domingos, I. Gaubeur, Z. Wang, C. Chen, M. R. Sardela, J.S. Souza, J. Am. Chem. Soc. 107 (2023) 995.
[27] X. Yan, Z. Wu, P. Yang, Y. Fu, W. Ma, Y. Zhao, B. Liu, Y. Mao, H. Shen, Mater. Res. Express. L. Jia 6 (2019) 086212.
[28] Z. Wang, J. Lv, J. Zhang, K. Dai, C. Liang, Appl. Surf. Sci. 430 (2018) 595.
[29] R. Venkatesan, S. Velumani, K. Ordon, M. Makowska-Janusik, G. Corbel, A. Kassiba, Mater. Chem. Phys. 205 (2018) 325.
[30] N. Ekthammathat, A. Phuruangrat, S. Thongtem, T. Thongtem, Russ. J. Phys. Chem. 92 (2018) 1036.
[31] S. Moscow, K. Jothivenkatachalam, J Mater Sci: Mater Electron. 27 (2016) 1433.
[32] H. Dong, X. Guo, C. Yang, Z. Ouyang, Appl. Catal. B: Environ. 230 (2018) 65.
[33] S. Renukadevi, A.Pricilla Jeyakumari, J Mater Sci: Mater Electron 32 (2021) 25399.
[34] Sharma, A.; Varshney, M.; Chae, K.H.; Won, S.O.; Curr. Appl. Phys. 18 (2018) 1458.
[35] I.M. Szilágyi, B. Fórizs, O. Rosseler, Á. Szegedi, P. Németh, P. Király, G. Tárkányi, B. Vajna, K. Varga-Josepovits, K. László, A.L. Tóth, P. Baranyai, M. Leskelä, J. Catal. 294 (2012) 119.
[36] G.N. Kustova, Y.A. Chesalov, L.M. Plyasova, I.Y. Molina, A.I. Nizovskii, Vib. Spectrosc. 55 (2011) 235.
[37] D. Nunes, A.R. Fragoso, T. Freire, M. Matias, A.C. Marques, R.F.P. Martins, E. F. Fortunato, A. Pimentel, pss RRL 15 (2021) 2100196.
[38] P. Makuła, M. Pacia, W. Macyk, J. Phys. Chem. Lett., 23, 2018, p. 6814.
[39] N.A. Mohamed, J. Safaei, A.F. Ismail, M.N. Khalid, M.F.A.M. Jailani, M.F.M. Noh, N.A. Arzaee, D. Zhou, J.S. Sagu, M.A.M. Teridi, Mater. Res. Bull. 125 (2020) 110779.
[40] Duan, S.F.; Tao, C.L.; Geng, Y.Y.; Yao, X.Q.; Kang, X.W.; Su, J.Z.; Rodríguez-Gutiérrez, I.; Kan, M.; Romero, M.; Sun, Y.; Zhao, Y-X.; Qin, D-D.; Yan, Y.; Chemcatchem 11 (2019) 729.
[41] F.U. Islam, N.H. Liton, H.T. Islam, M. Al Helal, M. Kamruzzaman, Chinese Phys. B. 26 (2017) 036301.
[42] S. Tian, X. Zhang, Z. Zhang, Desalination 479 (2020) 114348.
[43] W. Guo, K. Fan, J. Zhang, C. Xu, Appl. Surf. Sci. 447 (2018) 125.
[44] L. Yang, X. Liu, Z. Liu, C. Wang, G. Liu, Q. Li, X. Feng, Ceram. Int. 44 (2018) 20613.
[45] X. Wan, M.A. Khan, F. Wang, M. Xia, W. Lei, S. Zhu, C. Fu, Y. Ding, Chem. Eng. Res. Des. 152 (2019) 95.
[46] Abazari, R.; Mahjoub, A.R.; Salehi, G.; J. Hazard. Mater. 365 (2019) 921.
[47] G. Zhao, M. Wang, X. Cao, Y. Guo, W. Liu, H. Teng, Res Chem Intermed 46 (2020) 1487.
[48] S. Ullah, A.A. Khan, A. Jan, S.Q. Aain, E.P.F. Neto, Y.E. Serge-Correales, R. Parveen, H. Wender, U.P. Rodrigues-Filho, S.J. Ribeiro, Colloids Surf. A: Physicochem. Eng. Asp. 600 (2020) 124946.
[49] C.H. Claudino, M. Kuznetsova, B.S. Rodrigues, C. Chen, Z. Wang, M. Sardela, J. S. Souza, Mater. Res. Bull. 125 (2020) 110783.
[50] C. Murugan, R. A. Nataraj, M. P. Kumar, S. Ravichandran, A. Pandikumar, ChemistrySelect 4 (2019) 4653.
[51] Y. Liu, A. Yuan, Y. Xiao, H. Yu, X. Dong, Ceram. Int. 46 (2020) 16157.
[52] V. Jayaraman, C. Ayappan, A. Mani, Chemosphere 287 (2022) 132055.
[53] B. Purohit, S. Kumawat, A. Dixit, Mater. Res. Express. 5 (2018) 024001.
[54] M.F.R. Samsudin, P.J. Jayabalan, W.-J. Ong, Y.H. Ng, S. Sufian, J. Photochem. Photobiol. A: Chem. 378 (2019) 46.
[55] Y. Deng, L. Tang, G. Zeng, J. Wang, Y. Zhou, J. Wang, J. Tang, L. Wang, C. Feng, J. Colloid. Interface Sci. 509 (2018) 219.
[56] M. Song, Y. Wu, X. Wang, M. Liu, Y. Su, J. Colloid. Interface Sci. 529 (2018) 375.
[57] H.J. Kong, K.-H. Kim, S. Kim, H. Lee, J.K. Kang, J. Mater. Chem. A 7 (2019) 26279.
[58] M.S.L. Rosa, T. Knoerzer, F.C. Figueiredo, J.R. Santos Júnior, Polimeros 30 (2020) e2020004.
[59] A. Cárdenas, A. Vázquez, S. Obregón, M.A. Ruíz-Gómez, V. Rodríguez-González, Mater. Res. Bull. 142 (2021) 111385.
[60] A.Z. Hang, B.B. Liu, C.Q. Zhang, D.L. Feng, E.Q. Zhang, F.Z. Lv, G.Z. Zhang, AIP Advances 11 (2021) 125109.
[61] H.E.A. Mohamed, S. Afridi, A.T. Khalil, T. Zohra, M.M. Alam, A. Ikram, Z. K. Shinwari, M. Maaza, AMB Expr. 9 (2019) 200.

[62] X. Yuan, S. Qu, X. Huang, X. Xue, C. Yuan, S. Wang, L. Wei, P. Cai, Chem. Eng. J. 416 (2021) 129148.
[63] N.E. Mircescu, M. Oltean, V. Chiș, N. Leopold, Vib. Spectrosc. 62 (2012) 165.
[64] P. Praus, L. Svoboda, M. Ritz, I. Troppová, M. Šihor, K. Kočí, Mater. Chem. Phys. 193 (2017) 438.
[65] J. Liu, H. Wang, S. Wang, H. Yan, Mater. Sci. Eng.: B 104 (2003) 36.
[66] A. Massoud, S.B. Challan, N. Maziad, J. Macromol. Sci., Part A 58 (2021) 408.
[67] S.I. Boyadjiev, V. Georgieva, N. Stefan, G.E. Stan, N. Mihailescu, A. Visan, I. N. Mihailescu, C. Besleaga, I.M. Szilágyi, Appl. Surf. Sci. 417 (2017) 218.
[68] N.A. Mohamed, J. Safaei, A.F. Ismail, M.N. Khalid, M.F.A. Mohd Jailani, M.F. M. Noh, N.A. Arzaee, D. Zhou, J.S. Sagu, M.A.M. Teridi, Mater. Res. Bull. 125 (2020) 110779.
[69] J. Cheng, X. Yan, Q. Mo, B. Liu, J. Wang, X. Yang, L. Li, Ceram. Int. 43 (2017) 301.
[70] C. Adler, S. Selim, I. Krivtsov, C. Li, D. Mitoraj, B. Dietzek, J.R. Durrant, R. Beranek, Adv. Funct. Mater. 31 (2021) 2105369.
[71] R. Huo, X.-L. Yang, J.-Y. Yang, S.-Y. Yang, Y.-H. Xu, Mater. Res. Bull. 98 (2018) 225.
[72] M. Xu, Y. Zhu, J. Yang, W. Li, C. Sun, Y. Cui, L. Liu, H. Zhao, B. Liang, J. Am. Ceramic Soc. 104 (2021) 3004.
[73] F. Carvalho, E. Liandra-Salvador, F. Bettanin, J. Souza, P. Homem-de-Mello, A. Polo, Inorganica Chim. Acta. 414 (2014) 145.
[74] Y. Zhang, Q. Pan, G. Chai, M. Liang, G. Dong, Q. Zhang, J. Qiu, Scientific Reports 3 (2013) 1943.
[75] Z. Zhao, Z. Wu, X. Lin, F. Han, Z. Liang, L. Huang, M. Dai, D. Han, L. Han, L. Niu, Food Chem. 402 (2023) 134258.
[76] C.H. Claudino, B. S. Rodrigues, I. M. Factori, J.S. Souza, ChemistrySlect. 9 (2024) e202400076.
[77] J. Kang, Y. Tang, M. Wang, C. Jin, J. Liu, S. Li, Z. Li, J. Zhu, J. Environ. Chem. Eng. 9 (2021) 105524.